Physics of the Earth and Planetary Interiors 276 (2018) 118–133

Contents lists available at ScienceDirect

Physics of the Earth and Planetary Interiors

journal homepage: www.elsevier.com/locate/pepi

# Combining virtual observatory and equivalent source dipole approaches to describe the geomagnetic field with Swarm measurements

Diana Saturnino [a,*,1], Benoit Langlais [a], Hagay Amit [a], François Civet [a], Mioara Mandea [b], Éric Beucler [a]

[a] Laboratoire de Planétologie et Géodynamique, UMR 6112, CNRS et University of Nantes, Faculté des Sciences et Techniques, 2 rue de la Houssinière, BP 92208, 44322 Nantes Cedex 3, France
[b] Centre National d'Études Spatiales, 2 Place Maurice Quentin, 75039 Paris, France

ARTICLE INFO

*Article history:*
Received 23 November 2016
Received in revised form 11 May 2017
Accepted 6 June 2017
Available online 13 June 2017

*Keywords:*
Geomagnetic field
Virtual observatories
Swarm magnetic data
Equivalent Source Dipole (ESD)
Secular variation

ABSTRACT

A detailed description of the main geomagnetic field and of its temporal variations (i.e., the secular variation or SV) is crucial to understanding the geodynamo. Although the SV is known with high accuracy at ground magnetic observatory locations, the globally uneven distribution of the observatories hampers the determination of a detailed global pattern of the SV. Over the past two decades, satellites have provided global surveys of the geomagnetic field which have been used to derive global spherical harmonic (SH) models through some strict data selection schemes to minimise external field contributions. However, discrepancies remain between ground measurements and field predictions by these models; indeed the global models do not reproduce small spatial scales of the field temporal variations. To overcome this problem we propose to directly extract time series of the field and its temporal variation from satellite measurements as it is done at observatory locations. We follow a Virtual Observatory (VO) approach and define a global mesh of VOs at satellite altitude. For each VO and each given time interval we apply an Equivalent Source Dipole (ESD) technique to reduce all measurements to a unique location. Synthetic data are first used to validate the new VO-ESD approach. Then, we apply our scheme to data from the first two years of the Swarm mission. For the first time, a 2.5° resolution global mesh of VO time series is built. The VO-ESD derived time series are locally compared to ground observations as well as to satellite-based model predictions. Our approach is able to describe detailed temporal variations of the field at local scales. The VO-ESD time series are then used to derive global spherical harmonic models. For a simple SH parametrization the model describes well the secular trend of the magnetic field both at satellite altitude and at the surface. As more data will be made available, longer VO-ESD time series can be derived and consequently used to study sharp temporal variation features, such as geomagnetic jerks.



## 1. Introduction

The Earth's main magnetic field changes its strength and direction in time and space, with its temporal variation termed secular variation (SV). Knowledge and detailed description of the SV are essential to constrain the fluid dynamics just below the core-mantle boundary (CMB) and the coupling mechanism between the core and the mantle (e.g. Holme, 2015). Secondary sources of the geomagnetic field are the magnetised crust (crustal field) and the electrical currents in the ionosphere and magnetosphere, known as the external field. While the crustal field is static, external fields caused by the interaction between the main field and the solar wind vary on a broad range of time scales. The magnetospheric ring current, flowing at distances of a few Earth radii (e.g. Maus and Lühr, 2005), and the ionospheric currents flowing around 100 km altitude (e.g. Briggs, 1984) are examples of sources of short-term variations. The polar regions are dominated by the field-aligned currents (FAC), flowing along field lines of the ambient field and connecting the magnetosphere and ionosphere (e.g. Gjerloev et al., 2011; Lühr et al., 2015, and references therein). Ionospheric and magnetospheric currents also induce electrical currents in Earth's lithosphere and mantle (e.g. Langel and Estes, 1985; Kuvshinov and Olsen, 2006; Civet et al., 2015). The magnetic field measured at the Earth's surface or at satellite altitude is the superposition of all these sources.

* Corresponding author.
*E-mail address:* saturnino@space.dtu.dk (D. Saturnino).
[1] Present address: DTU Space, Diplomvej, Building 371, 2800 Kgs. Lyngby, Denmark.

http://dx.doi.org/10.1016/j.pepi.2017.06.004
0031-9201/

Since the mid-19th century, the strength and direction of the magnetic field have been continuously measured at ground magnetic observatories, locally constraining the SV. However, the limited number of observatories and their uneven distribution across the globe (e.g. Bloxham et al., 1989; Brown et al., 2013) hampers the determination of SV global patterns with high spatial resolution. For the last two decades scientific satellite missions have been providing high-precision magnetic field observations at a global scale. Such missions, like the Danish satellite Ørsted (Neubert et al., 2001) and the German satellite CHAMP (Reigber et al., 2002) provided almost continuously magnetic field measurements with global coverage. The ESA's Swarm mission (Friis-Christensen et al., 2006) was launched on 22 November 2013. It consists of a constellation of three identical satellites in polar orbit at different altitudes. Two of them (A and C) fly almost side-by-side around 460 km altitude and the third satellite (B) flies about 55 km higher (Fig. 1). The phase shift increases with time allowing the constellation to survey all local times during its nominal lifetime (Olsen et al., 2006). The constellation delivers simultaneous magnetic measurements at two different altitudes. Two magnetic instruments operate on each satellite boom, a Vector Fluxgate Magnetometer (VFM), which is combined with a Star Tracker, delivers vector geocentric measurements, and an Absolute Scalar Magnetometer (ASM) providing very accurate 1 Hz absolute scalar measurements for both VFM calibration and scientific studies (Fratter et al., 2016).

Magnetic field observations at satellite altitude and with global coverage have allowed the construction of improved global field models using spherical harmonics (SH). These models must account for external field contributions, unless they are a priori minimised. When using ground observatory measurements only annual or monthly means are usually considered (e.g. Jackson et al., 2000; Wardinski and Holme, 2006). This aims at averaging out the short-term temporal variations of the external field, thus filtering out a large part of geomagnetic variability of external origin. When using satellite measurements a strict data selection is done to keep only quiet, local night-time measurements. This selection is performed according to magnetic activity indices such as the Dst (e.g. Sugiura, 1964). This reduces the external fields but also strongly reduces the amount of available data for the inversion (Olsen et al., 2007).

A direct comparison between ground observations and satellite data is difficult due to the very different nature of the measurements. Similarly, it is not possible to directly study the SV and its spatial patterns with satellite data as with ground observatories. Depending on the satellite's orbital geometry, the revisiting period for a particular location ranges between days and months, while at ground observatories measurements are acquired at a constant location (Turner and Rasson, 2007). Satellite magnetic measurements are also taken at different, possibly time-dependent, altitudes. As the satellite orbit altitude naturally decreases with time (e.g. Maus et al., 2007), this leads to an artificial increase of the measured magnetic field intensity and to a false apparent secular variation.

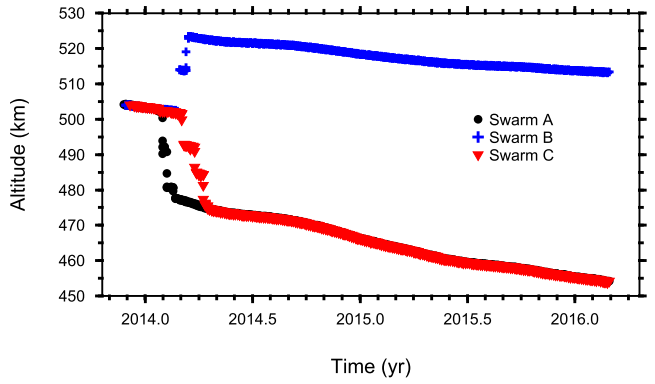


**Fig. 1.** Daily mean altitude of the three Swarm satellites from November 2013 to February 2016.

A different approach to describe the magnetic field, based on Virtual Observatories (VO), was proposed by Mandea and Olsen (2006). It consists in directly extracting the SV information from satellite data as it is done at ground observatories. A VO is defined as a volume inside which all available satellite measurements during a given time period are taken into account. Olsen and Mandea (2007) considered five years of CHAMP measurements to construct a global grid of 5° equally spaced VOs. The measurements acquired during one month and inside a cylindrical volume were corrected to a constant altitude. The correction assumes that the measurement residuals (obtained by the subtraction of an a priori known SH field model) are given by a potential field which varies linearly in space. Parameters are estimated and used to compute a mean magnetic field residual for each month and VO. They assumed that over 1-month interval the contributions of external origin to the measured field can be neglected. The obtained VO time series were found to have a very good correlation with the corresponding ground-based observatory time series (Mandea and Olsen, 2006).

Here, we follow and expand the approach of the VOs, but without using an a priori model to perform the data correction for the variable altitude. Instead, we use the Equivalent Source Dipole (ESD) technique (Mayhew, 1979; Langlais et al., 2004) to locally reduce the measurements to a constant altitude at a mean time. We place dipoles inside the Earth in order to model the internal field, i.e., the field associated with sources below the satellites. Another novelty comes from the new data from the Swarm constellation, with three satellites providing simultaneous measurements at three different locations for the first time.

The paper outline is as follows. In Section 2 we present our modified virtual observatory scheme. It is tested and validated on synthetic data in Section 3. In Section 4 the approach is applied to Swarm measurements. A comparison between ground-based observatory time series and respective VO-ESD time series is performed and a global and homogeneous mesh of VO time series is constructed. These time series are inverted for SH global main field models is Section 5, before concluding remarks in Section 6.

## 2. The VO-ESD approach

The objective of the VO-ESD approach is to compute time series of internal magnetic field values at a specific location at satellite altitude, using all available nearby measurements. This is similar to how magnetic observatory monthly mean values are computed.

All measurements made inside a VO volume and during a given time interval are considered. We do not attempt to remove the external field variations (by means of a priori data selection using external activity indices), nor to explicitly model and describe the external field. A magnetic field value at the VO location and chosen altitude is obtained by the Equivalent Source Dipole technique, in which we use dipoles placed near the core-mantle boundary. A global mesh of VO time series can then be built. We describe below the different elements of this technique.

### 2.1. Virtual observatory (VO) concept

#### 2.1.1. Spatial and temporal extent

In order to define a virtual observatory at satellite altitude we consider all Swarm measurements acquired inside a cylindrical volume during a given time period. The cylinder radius and the

considered time interval are chosen to fulfil the following requirements. The volume has to be large enough and the time interval long enough to contain sufficient data to constrain the equivalent magnetisation (see Section 2.2). The volume has to be small enough so that the spatial variations of the field are limited. Finally, the considered time interval has to be short so that the temporal variation of the core field is small and can be neglected. From these constraints we choose a cylindrical volume with 1.5° (or 167 km) radius at the surface of the Earth. Measurements are selected only if their horizontal distance to the axis of the cylinder are less than or equal to this value (Fig. 2). Periods of 30 days are considered.

Satellite measurements are acquired at different altitudes due to satellite trajectories (Fig. 1). To obtain a time series of magnetic field values as one would obtain at a ground observatory, a correction has to be made to bring the measurements to a constant altitude. This altitude correction is made by applying the Equivalent Source Dipole technique for each time interval and VO data volume (see Section 2.2).

### 2.1.2. Global mesh

A global mesh of VO at spacecraft altitude is defined as follows. To obtain an approximately equal area mesh (Fig. 3), the VO centres are separated in latitude by 2.5° and define 72 latitudinal bands, with $\vartheta_{vo} = \pm 1.25^\circ, \pm 3.75^\circ, \pm 6.25^\circ, \ldots, \pm 88.75^\circ$. In each band, the longitude $\phi_{vo}$ of each VO and the number of longitudinal divisions, $N_{\vartheta_{vo}}$ (rounded up to the nearest integer), are chosen so that:

$$N_{\vartheta_{vo}} = \frac{360}{2.5} \cos \vartheta_{vo} \tag{1}$$

Hence, immediately north and south of the equator there are 144 virtual observatories, at $\vartheta_{vo} = \pm 48.75^\circ$ there are 95 and at $\vartheta_{vo} = \pm 86.25^\circ$ only 10. The resulting mesh contains 6644 VOs. This equal area mesh is preferred over an equiangular one mainly because the latter would introduce a too strong latitudinal dependency for the number of measurements per VO volume. Fig. 3 displays the locations of all virtual observatories in the mesh.

### 2.2. Equivalent Source Dipole (ESD) technique

The ESD technique was introduced to analyse satellite magnetic field data acquired on irregular surfaces (Mayhew, 1979). It has been widely used to reduce data collected at different altitudes to a common elevation over a small area in order to, for example, derive crustal field anomaly maps at a given altitude (Purucker et al., 1996; Dyment and Arkani-Hamed, 1998; Langlais et al., 2004; Langlais and Purucker, 2007). The method is based on the expression of a magnetic anomaly caused by a magnetic dipole. Considering the magnetic moment **M** of a dipole located at $(r_d, \theta_d, \phi_d)$, and that there are no sources between the dipole and a magnetic observation located at $(r, \theta, \phi)$, where $r$ is the radius and $\theta$ the co-latitude, the observed magnetic potential is expressed as

$$V = -M \cdot \nabla \frac{1}{l}. \tag{2}$$

The distance $l$ between the dipole and the observation location is

$$l = (r_d^2 + r^2 - 2 r_d r cos(\zeta))^{\frac{1}{2}}, \tag{3}$$

with $\zeta$ being the angle between observation and dipole locations,

$$cos(\zeta) = cos(\theta) cos(\theta_d) + sin(\theta) sin(\theta_d) cos(\phi - \phi_d). \tag{4}$$

The magnetic field at the observation point due to a single dipole is given by

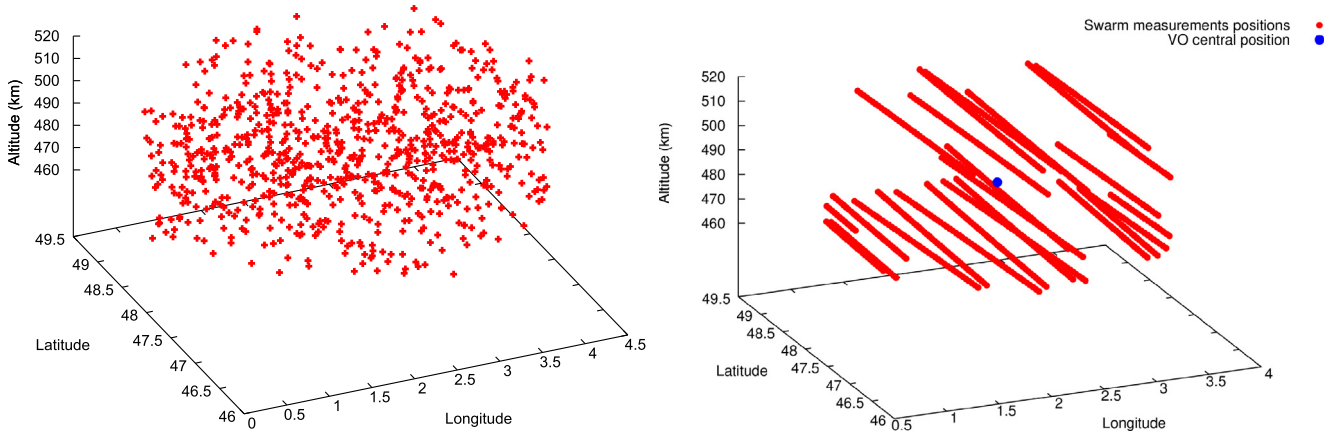


**Fig. 2.** Example of the data distribution within a cylindrical VO volume of 1.5° radius centred at the location of the ground magnetic observatory of Chambon-la-Forêt, France (CLF, 2.26°E 47.83°N) and for a 30-day period, with (left) a random spatial distribution and (right) mimicking Swarm orbits positions.

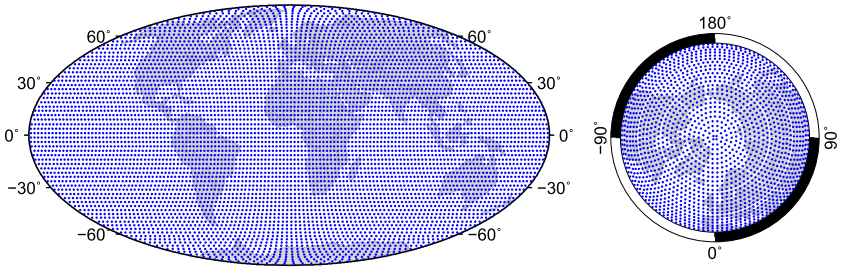


**Fig. 3.** (Left) Global mesh of virtual observatories. (Right) Polar view of the northern hemisphere, with $30^\circ \leqslant \vartheta_{vo} \leqslant 90^\circ$.

$$\mathbf{B} = -\nabla V = -\left(\frac{\partial V}{\partial r}, \frac{1}{r}\frac{\partial V}{\partial \theta}, \frac{1}{r\sin(\theta)}\frac{\partial V}{\partial \phi}\right). \quad (5)$$

The magnetic field at a given location is the sum of all magnetic fields created by all equivalent dipoles, placed at some depth. Then, using measured magnetic components ($X$, the horizontal northward component; $Y$, the horizontal eastward component; and $Z$ the vertical component positive towards the Earth's interior) the equivalent magnetisation $(M_X, M_Y, M_Z)$ for each dipole of the mesh is computed by a least-squares fit in an iterative, conjugate gradient, inversion scheme (Purucker et al., 1996) (see Section 2.3). The forward (or direct) scheme (following Eq. (2)) is used to predict a magnetic field value at the VO location and for a given time period, using the magnetisation of all equivalent dipoles.

There are different solutions (or iterations) of dipole magnetisations that can explain almost identically the observed magnetic measurements. This non-uniqueness forces a careful selection of the ESD modelling technique parameters which have to be a priori chosen. These are the number of dipoles ($N_{dip}$), the geometry and spatial extent of the dipole mesh, and the depth at which they are placed. The assumed thickness of the dipole mesh (corresponding to the thickness of the equivalent magnetised layer, which in this case does not have a physical meaning) does not significantly affect the results as only the vertically integrated magnetisation is actually computed (Langlais et al., 2004). On the other hand, to avoid numerical instabilities related to artificial lateral variations of the magnetisation, we use ESDs on a mesh which is as homogeneous as possible (e.g. Covington, 1993; Purucker et al., 1996; Katanforoush and Shahshahani, 2003).

We ran several tests on the dipole mesh parameters. We placed dipoles at different depths and found that the most consistent results were obtained for a depth of 2900 km (approximately the depth of the CMB). After a series of tests, the following parameters were chosen. The dipole mesh has a hexagonal geometry and it is centred below the VO centre location. It contains $N_{dip} = 91$ dipoles which are separated from each other with a mean distance of $d = 18^\circ$ (Fig. 4).

### 2.3. Inversion

The inverse problem can be written as (Purucker et al., 1996):

$$\mathbf{b} = \mathbf{D}\mathbf{x} + \boldsymbol{\nu}, \quad (6)$$

where $\mathbf{b}$ is the vector containing $3 \times N_{obs}$ magnetic field observations; $\mathbf{x}$ the vector containing $3 \times N_{dip}$ magnetisation components to be determined; $\mathbf{D}$ the geometric source function matrix relating $\mathbf{x}$ to $\mathbf{b}$; and $\boldsymbol{\nu}$ the observation noise vector (of zero mean). This is solved by seeking to minimize the quantity $\mathbf{L}(\mathbf{x}) = \boldsymbol{\nu}^T\boldsymbol{\nu}$, which corresponds to solving $\mathbf{D}^T\mathbf{D}\mathbf{x} = \mathbf{D}^T\mathbf{b}$. The minimum is reached when $\nabla\mathbf{L} = \mathbf{D}\mathbf{x} - \mathbf{b}$ tends to zero (Press et al., 1992). We use the conjugate gradient iterative method (Shewchuk, 1994), which at each iteration $k$ gives a new solution written as

$$\mathbf{x}_{k+1} = \mathbf{x}_k + \alpha_k\mathbf{p}_k, \quad (7)$$

where $\mathbf{p}_k$ is a direction search vector and $\alpha_k$ a scalar that minimizes $\mathbf{L}(\mathbf{x}_{k+1})$ along the direction of $\mathbf{p}_k$, with

$$\alpha_k = \frac{\mathbf{r}_k^T\mathbf{r}_k}{\mathbf{p}_k^T\mathbf{D}^T\mathbf{D}\mathbf{p}_k}, \quad (8)$$

where $\mathbf{r}_k$ are the residuals after the $k$th iteration. The change from $\mathbf{r}_k$ to $\mathbf{r}_{k+1}$ is conjugated or perpendicular to all preceding search directions $\mathbf{p}_k$. The root mean square (rms) residual between observed and predicted field component $C$ is computed for each iteration as

$$\sigma_{C_k} = \sqrt{\frac{\sum_{i=1}^{N_{obs}}(C_i - C_{i,k})}{N_{obs}}}. \quad (9)$$

$C_i$ and $C_{i,k}$ are the measured and predicted magnetic component at the location of observation $i$. The rms residuals for the three vector components and for the scalar field are computed after each iteration and used as a convergence criterion. The numerical inversion is stopped when $\sigma_k < 10^{-10}$ nT or after 100 iterations whichever comes first. Both this number of iterations and low $\sigma_k$ limit are purposely chosen so that an a posteriori choice of the iteration number can be made.

For each VO volume and time period i.e., for each inversion, the rms residuals relative difference between each iteration $k$ and the previous $k-1$ is computed for $F$ (field intensity, computed from the three field components, $F = \sqrt{X^2 + Y^2 + Z^2}$),

$$\frac{\sigma_{F_k} - \sigma_{F_{k-1}}}{\sigma_{F_k}} \times 100. \quad (10)$$

The iteration for which this difference becomes smaller than 1.5 % is chosen (this limit was determined empirically). When the difference is smaller than this value, the $(k+1)^{th}$ solution does not significantly change with respect to the previous $k^{th}$ one. We noted that each distinct time period may result in a different iteration number, but that one particular number was more frequent for each VO. For consistency and to avoid possible artificial temporal jumps between successive solutions due to the different iteration numbers, we decided to choose the most frequent iteration number for all periods for a given VO. Then the estimated equivalent magnetisation distribution is used to predict the magnetic field components at the VO location $(\vartheta_{vo}, \phi_{vo})$ and at 490 km altitude. This altitude corresponds to the mean altitude of all Swarm mea-

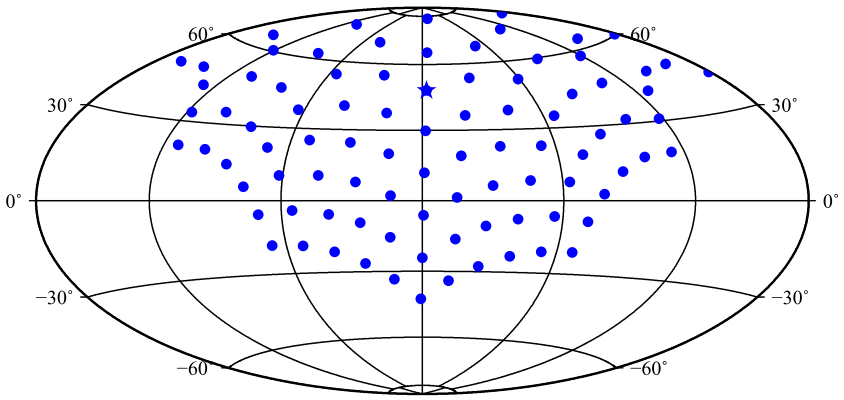


**Fig. 4.** Example of a hexagonal dipole grid, with 91 dipoles and 18° of mean distance between each dipole, centred below the CLF observatory location (star).

surements taken within the considered VO volume and period. The obtained VO prediction is compared with the values given by the global SH field model used to generate the synthetic input data (see below). For each period the difference $(\Delta X, \Delta Y, \Delta Z)$ between the SH model prediction $(C_{SH})$ and the VO-ESD prediction $(C_{VO-ESD})$ is computed as:

$$\Delta C = C_{SH} - C_{VO-ESD}. \quad (11)$$

This difference should be as close as possible to zero.

An inversion is performed for every period and VO. This corresponds to estimating 273 parameters $(3 \times N_{dip})$ for each period.

## 3. Data and validation

### 3.1. Data

We apply the VO-ESD approach to Swarm data, from the beginning of the mission on 26/11/2013 until 26/2/2016 (Swarm dataset). The data consists of the release by ESA of Swarm vector field measurements $(X, Y, Z)$ with 1 Hz sampling rate (ESA L1 product, baseline 0408/0409).

Swarm measurements are released with four flags, Flag_B, Flag_F, Flag_q and Flag_platform. These flags are associated with VFM, ASM, attitude and telemetry information, respectively (Tøffner-Clausen, 2013). Based on such flags a selection of data was performed:

- Flags_B: 0 or 1 (VFM is nominal or ASM is turned off), or 255 after 2/11/2014;
- Flags_F: 0 or 1 (ASM is nominal or running in Vector mode);
- Flags_q: between 0 and 6, or between 16 and 22 (at least two Camera Head Units nominal);
- Flags_Platform: 0 or 1 (nominal telemetry or thrusters not activated).

The excluded measurements correspond to moments when at least one of the instruments has degraded performance or it is turned off. Note that the ASM instrument on Swarm C stopped providing data after 5 November 2014. This resulted in data files from this satellite with the Flag_B always equal to 255. In this case, the satellite data was also considered for the dataset.

The time series we compute are also compared to ground time series. For that purpose we use ground magnetic field measurements acquired at magnetic observatories, termed Ground dataset. For this dataset we compute 30-day mean values at selected INTERMAGNET observatories, from their 1-minute values. Means are defined as an average of all measurements available for these days. This is slightly different from the commonly defined monthly mean values which are associated with varying durations between 28 and 31 days. Eight ground observatories are considered, six in the European area and two in the Southern Hemisphere. The six European observatories are chosen because they are close to each other, allowing time series obtained at nearby locations at satellite altitude to be compared. The other two are chosen as examples from the Southern Hemisphere and close to the magnetic pole, where external currents contributions, such as FAC, are important.

For the validation scheme (see subsections below) synthetic datasets are used. A global geomagnetic field model (Olsen et al., 2014), based on a spherical harmonic expansion up to degree 13, is used to predict both synthetic satellite measurements and synthetic time series at the VO location. These input magnetic field predictions are time dependent and account for the SV, unless noted.

The first synthetic dataset, Synthetic dataset 1, consists of a VO data volume centred above the Chambon-la-Forêt magnetic observatory (CLF) location ($\vartheta_{vo} = 47.83^\circ, \phi_{vo} = 2.26^\circ$), and $r_{vo} = 490$ km. The data points within the VO cylinder are randomly distributed in latitude, longitude and altitude, with altitudes varying between 463 and 517 km, similar to the two main Swarm altitudes (Figs. 1 and 2). Several consecutive 30-day time intervals are considered and a different cylinder is generated for each one. Due to the variable data locations each cylinder has a different spatial distribution. Tests are made with and without adding white noise generated by a random process to the data, with amplitudes equal to 5 or 10 nT, and corresponding to standard deviations of 2.9 and 5.8 nT, respectively.

Synthetic dataset 2 consists of magnetic field values predicted along Swarm orbit locations during the first thirteen months of the mission (from November 2013 to December 2014), and selected using the above mentioned flags. Fig. 2 shows an example of the spatial distribution of Swarm orbits within a VO volume again at the same location as Synthetic dataset 1. For different periods the spatial distribution of the synthetic data points can change significantly, with $N_{obs}$ ranging from 437 to 1151. Tests are made with or without adding white noise, similarly to the Synthetic dataset 1 case.

### 3.2. Tests with synthetic data at random locations

In this and the following subsection, we present the results of tests we performed on the synthetic datasets to validate the VO-ESD approach. The validation scheme is presented in Fig. 5. The ESD technique is used to reduce all VO synthetic measurements within a 30-day period to a single magnetic vector value at the VO centre.

In this subsection, we present the results for the case with randomly distributed data over the VO, for Synthetic dataset 1, with or without noise. For the ideal case (i.e., without noise), $\sigma$ varies from 0.4 to 1.5 nT for the three magnetic components and field intensity. These rms residual values are significantly different from zero. This can be explained by (1) the spatial variation of the field within the VO volume and (2) the temporal variation of the field during the 30-day period. The temporal variation has the most important effect. This is confirmed with a test performed without taking into account SV to generate the predictions. In this case, $\sigma$ was smaller than 0.1 nT. When a noise is added (amplitude 5 nT) the rms residuals increase to about 3 nT, which is very close to the standard deviation of the added noise. Similar results are observed when noise of 10 nT is added, with rms residuals increasing to about 5.9 nT.

Fig. 6 shows the differences between the input field and that predicted by our approach (Eq. (11)) for the three magnetic components and twelve periods, for the cases without and with a 5 nT amplitude white noise. These differences are always within $\pm 0.1$ nT in the noise-free case. The smallest differences are found for the $Y$ component. When noise is added (5 nT amplitude), differences are larger but stay below $\pm 0.5$ nT, even when the rms residuals of the ESD inversion are of the order of 3 nT. The vertical component $\Delta Z$ shows slightly higher differences (more than 0.4 nT). The differences are always lower than $\pm 2.5$ nT when 10 nT amplitude noise is added (not shown). We conclude that the addition of noise to the data influences the final rms residuals and differences. However, the differences are still small considered the added noises, and always below $\pm 0.1$ nT without noise.

### 3.3. Tests with synthetic data along Swarm orbits

We next apply the VO-ESD approach to Synthetic dataset 2. Again, a prediction is obtained for every period at the centre of the VO. The obtained rms residuals are found to range from 0.1 to 1.3 nT, varying slightly for different periods. The $Y$ component

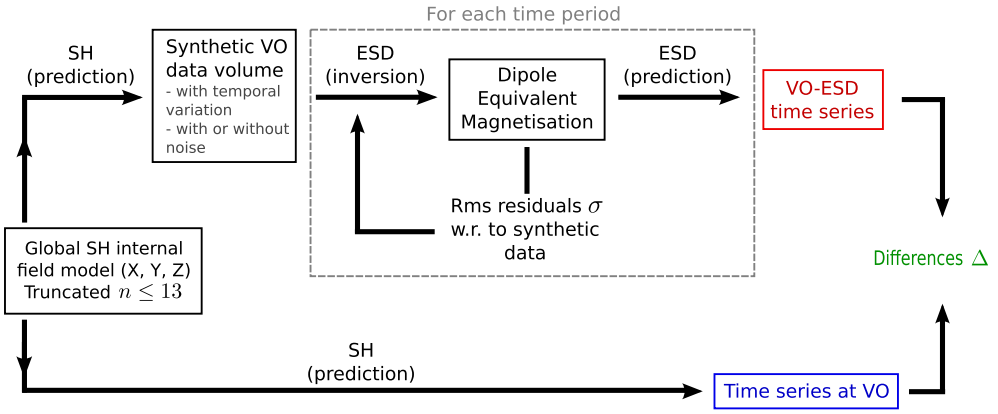


**Fig. 5.** Validation scheme of the VO-ESD approach. The starting point is shown on the left, with the input of an SH field model.

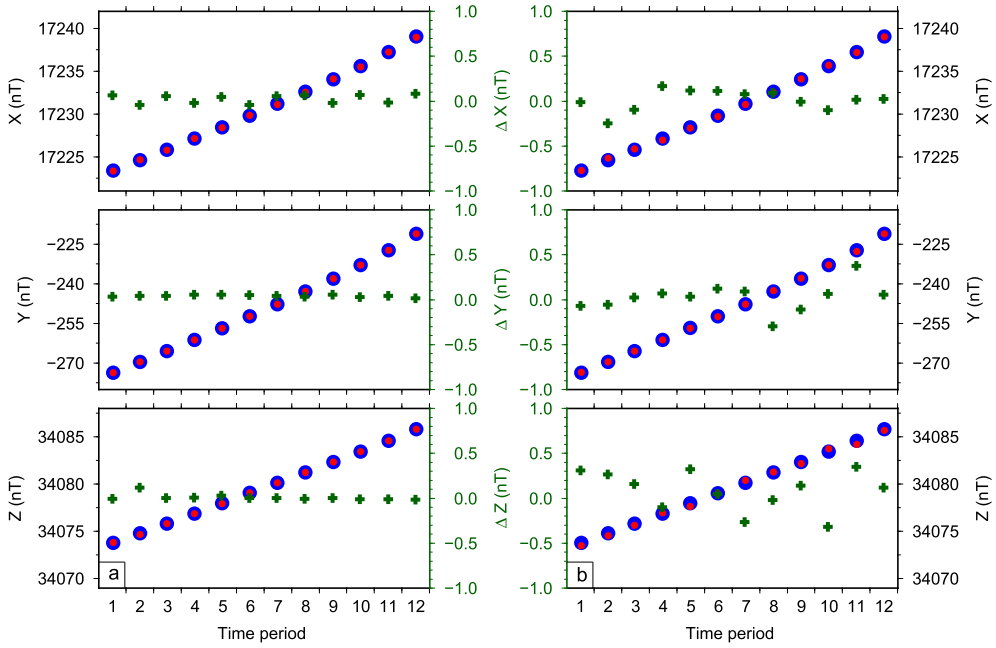


**Fig. 6.** VO-ESD predictions (red) for the three geomagnetic field components at the VO location for each 30-day period, (a) without and (b) with 5 nT white noise added. Also shown are the predictions of an SH model at the middle of the time period (blue) and the differences between the model and the VO-ESD predictions (green), with corresponding axis in green. (For interpretation of the references to colour in this figure caption, the reader is referred to the web version of this article.)

presents larger rms residuals than *X* and *Z*. As with the Synthetic dataset 1 (Section 3.2), rms residuals from all the periods lie inside a small interval, with no extreme values. Thus, they are not significantly affected by the spatial distribution of the orbit positions.

Tests are also made with white noise of 5 nT or 10 nT amplitude added. As expected, rms residuals increase with noise. For 5 nT amplitude white noise, rms residuals are of the order of 3.2 nT for the three magnetic components and 5.5 nT for the field intensity, which is consistent with the considered noise. Similar results are obtained for 10 nT amplitude noise.

Fig. 7a shows the differences between the field model and the VO-ESD prediction (Eq. (11)) for the thirteen periods. Differences vary from ±0.1 nT to ±0.5 nT. The *X* component exhibits the smallest differences (very close to zero), while *Z* presents the highest differences (closer to 0.5 nT). These differences remain small and confirm that the variable spatial distribution of the input data does not significantly affect the results.

The same result is found for the case of synthetic orbits with added noise (Fig. 7b). 5 nT amplitude white noise slightly increases the differences at the VO centre. Nevertheless, they remain smaller than ±0.7 nT. For 10 nT amplitude white noise (not shown) the differences increase to ±1.0 nT. However, this is still considered satisfactory.

The tests performed show that all satellite magnetic measurements, acquired within a VO volume and during a 30-day time interval, can be adequately reduced to a single magnetic field measurement at a mean fixed altitude by the VO-ESD approach. This approach can then be used to treat satellite magnetic field measurements, acquired at different altitudes, to obtain virtual observatory time series.

## 4. VO-ESD results

### *4.1. Application to selected locations and comparison with ground observatories*

Before applying the VO-ESD approach to a global mesh of VO, we first apply it to carefully selected locations and compare the

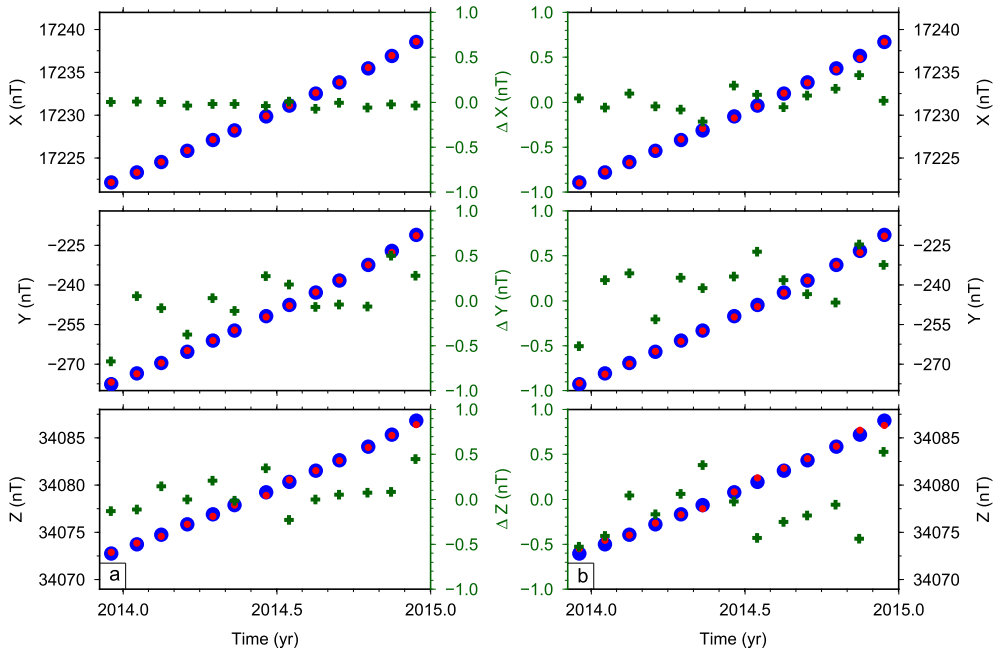


**Fig. 7.** VO-ESD predictions (red) for the three geomagnetic components at the VO location for each 30-day period, (a) without and (b) with 5 nT white noise added, for the case of synthetic data on Swarm orbits. Also shown are the predictions of an SH model at the middle of the time period (blue) and the differences between the model and the VO-ESD predictions (green), with corresponding axis in green. (For interpretation of the references to colour in this figure caption, the reader is referred to the web version of this article.)

derived VO time series to the corresponding ground observatories. The purpose is to investigate the agreement between temporal variations at the Earth's surface and at satellite altitude as recovered by the VO-ESD approach. For this comparison purpose, only ground based (Ground dataset) and Swarm measurements (Swarm dataset) acquired during 2014 are considered. Twelve periods of 30 days from the Swarm dataset are constructed to compare the resulting VO-ESD predictions with corresponding ground observatory 30-day means, constructed from the Ground dataset.

We first investigate the VO time series and associated statistics. The rms residuals (Eq. (9)) obtained for the eight considered VOs, for all time periods and field components are always larger than 2.5 nT. They can be as high as 189 nT (for $F$) for the DRV location, and 96 nT (for $F$) for the other seven locations. The rms residual mean values (for all eight locations) are 22.8, 21.9, 13.7 and 36.1 nT for $\sigma_X, \sigma_Y, \sigma_Z$ and $\sigma_F$, respectively. The VO above DRV presents the largest rms residuals, with minimum value of 12.8 nT. For some periods $\sigma$ for this VO is as large as 189 nT for $F$ and 153 nT for $Y$. These larger rms residuals may be related to the high latitudinal location of the VO. At high latitudes external field features such as FACs add significant contributions to the measured field. These contributions are not explicitly modelled by our approach, because we only consider internal sources, and make no parametrization for external sources. These larger values are thus not to be seen as a weakness of our approach. On the contrary they may prove that external fields do not enter into the model. This issue will be discussed further, in Section 5.2.

Fig. 8a to c presents the individual differences between each Swarm measurement and the corresponding ESD prediction, as a function of time and location, for three different VO locations. The nearby CLF and DOU VOs present similar time dependence of differences. The third VO on the Southern Hemisphere (DRV) displays higher differences than the other two examples. In DRV the horizontal components ($X$ and $Y$) present larger differences than $Z$ and $F$. Differences for $X$ and $Y$ can be as large as 530 nT, whereas for $Z$ and $F$ they are always under 130 nT.

All three VO examples show an increase of the differences around the 2nd, 3rd or 4th and also for the last period. At DRV, this time dependence of the differences is more clearly seen for $X$ and $Y$ than for $Z$ and $F$. The timing of these large differences may have two explanations, related to either geomagnetic field events or data quality. Fig. 8d shows the Dst geomagnetic index during 2014. Strong variations are visible over March, May and September. These variations correspond to events of enhanced solar activity and associated intensification of external field currents and the occurrence of geomagnetic storms (e.g. Le et al., 2016). This intensification of external field affected Swarm observations and as a consequence also the VO-ESD time series. This may be the cause for the larger residuals correlated in time for all three VOs seen around March and May. The event during September occurs prior to the large differences seen in the last periods, for the three VOs. The second reason for the observed time dependence may be the orbital manoeuvres on the three Swarm satellites. During the first months of the mission several manoeuvres were applied to the satellites, especially from the end of January to the beginning of March (see Fig. 1, see also https://earth.esa.int/documents/10174/1568455/Swarm_manoeuvres). These manoeuvres as well as torque corrections may have biased the magnetic measurements taken during that period.

30-day mean ground observatory time series are compared to those obtained by the VO-ESD approach in Fig. 9, showing comparable general trends. In CLF and DOU ground observatory time series, $X$ increases during the first half of the year, and then decreases until the end of the year. The corresponding VO-ESD time series reflects this change of behaviour at the middle of the year. However, the VO time series shows an increase followed by a decrease of the field of the $X$ component between the 9th and the 11th periods. This change in $X$ is not seen at CLF and DOU ground observatories time series. For the DRV ground observatory the $X$ time series behaves differently, with a slow decrease between the 2nd and the 10th periods. The VO-ESD derived time series for the same component and location shows more short-term variations with an

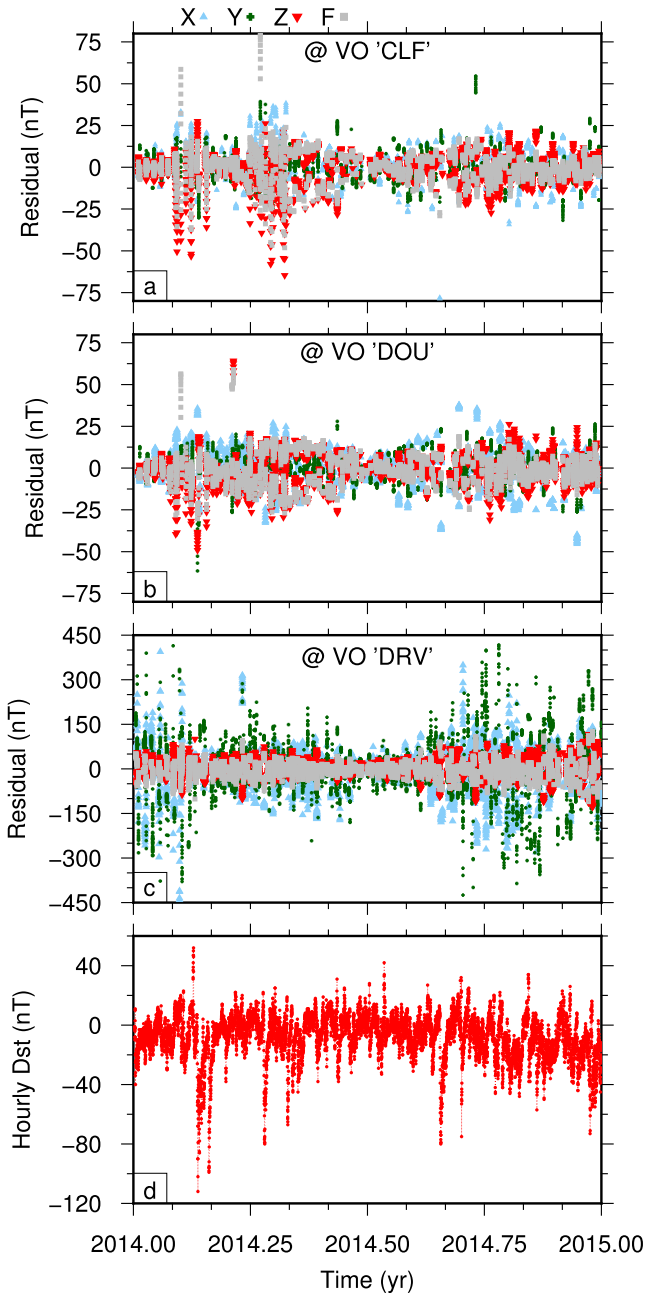


**Fig. 8.** Residuals (differences) between Swarm measurements and the corresponding ESD prediction at satellite altitude, for the three magnetic field components and field intensity, at three VOs above the ground observatories (a) CLF (Chambon-la-Forêt, France), (b) DOU (Dourbes, Belgium) and (c) DRV (Dumont d'Urvile, Antarctica); and (d) hourly Dst geomagnetic time series.

increase of the field during the 6th and the 7th periods, not seen at the ground. CLF and DOU show for both ground and VO-ESD time series an increase of *Y* over the entire year. At DRV, time series variations seem anti-correlated for *Y*, i.e., when *Y* decreases before the 6th period at satellite altitude, it increases at the ground, and conversely for the last two periods, with DRV *Y* ground values increasing and VO-ESD values decreasing.

The vertical component shows a similar behaviour at CLF and DOU ground observatories, with a small increase of the field during the first periods and a sharper increase from the 6th period until the last. At DRV the ground time series shows two decreases of the field during the first three periods and in the 8th. All VO-ESD *Z* time series show a sharp increase of the field during the last periods, as well as short-term variations of the field during the first eight periods. These are only partially correlated with DRV ground time series and not correlated with CLF and DOU time series. In general VO-ESD time series contain more short-term temporal variations than the corresponding ground time series.

Table 1 presents the Pearson's correlation coefficient (e.g. Press et al., 1992) between ground observatories and the corresponding VO-ESD time series. These correlations were also estimated between time series computed at the ground and at satellite VOs altitude from an SH model (the same one used during the validation process), without taking into account any external field. The obtained correlations (not shown) are larger than 0.999 for all three magnetic components. Any deviation from a perfect correlation could then be due to external field contributions affecting differently the VO time series and the ground time series. Generally, ground observatory and VO time series are strongly correlated. The *Y* component appears to be the most correlated, with correlation coefficients always equal or greater than 0.85, except for the DRV observatory. These smaller correlations for DRV may be related to the proximity to the magnetic pole, where the FACs significantly affect the horizontal components of the field. Correlations for the *X* component are low. Overall, higher latitude observatories are associated with smaller correlations with corresponding VO-ESD time series.

### 4.2. Geomagnetic field time series on a global mesh of VO-ESD

A global mesh of virtual observatories is constructed at satellite altitude by applying the VO-ESD approach described above to Swarm measurements. Time series of 27 magnetic values are derived at each VO location The full process thus involves 6644 VOs and 27 periods of 30 days, summing up to 179 388 inversions.

Due to the orbital manoeuvres which took place at the beginning of the mission (see Fig. 1), the range of altitudes of measurements during the first months does not comprise the mean altitude of the measurements after these manoeuvres (around 490 km). An inversion using the ESD technique should only be used to predict the field within the volume in which the actual observations were acquired. Thus, modelling the magnetic field at a constant altitude for all VOs for the first months of the Swarm mission is not adequate. Therefore, for each VO we search for an altitude which always lies (during the time interval of the available measurements) within the altitude range of the measurements during the first two months of the mission. The selected altitude is always within the altitude range of the following months of the mission. All predictions for a given VO are made for the chosen altitude. With this approach each VO has a different altitude, ranging between 482.56 and 507.19 km. The VOs altitude decrease from the Southern Hemisphere to the Northern Hemisphere.

Fig. 10 displays the rms residuals associated with each VO and period, as a function of VO (dipole) geomagnetic latitude. Both hemispheres present similar patterns. High latitude ($> |50|^\circ$) VOs show larger *X* and *Y* rms residuals. The difference between high latitudes and mid latitudes rms residuals is especially strong for *Y*. In general, rms minimum values increase when the VO centre location geomagnetic latitude is above $|70|^\circ$. The rms residuals for *Z* are larger at low latitudes, increasing towards the magnetic equator. For *F* there are large rms residuals both at equator and high latitudes. These observations may be explained first at polar latitudes by FACs, as these contributions dominate compared to those of the main field there. Around the magnetic equator, the ionospheric equatorial electrojet (EEJ) is associated with a day side structure (Baumjohann and Nakamura, 2007), which may explain the observed larger *Z* residuals.

Fig. 11 shows the VO-ESD time series obtained for four VOs, at different locations on the globe (and different altitudes). CHAOS-

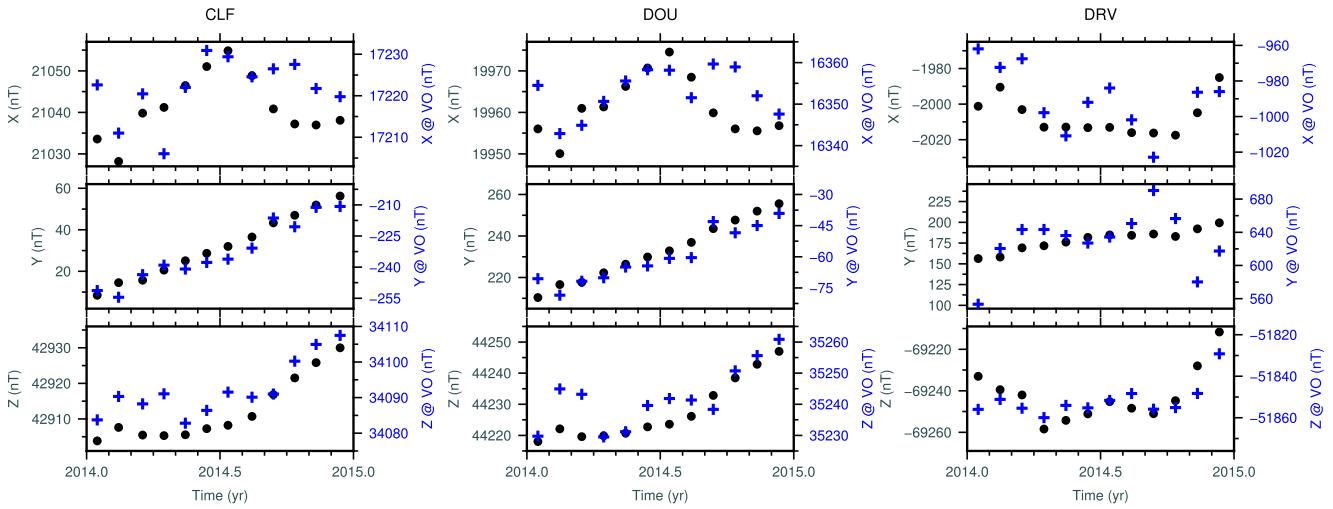


**Fig. 9.** 30-day mean value time series of the three magnetic components at CLF, DOU and DRV ground magnetic observatories (gray circles, left axis) and corresponding values given by the VO-ESD approach (blue pluses, right axis). Note that the difference between maximum and minimum in the vertical axis is the same both at the ground and satellite altitude, for each magnetic component and location.

**Table 1**
Ground magnetic observatories locations and the correlation coefficient ($\rho$) between their time series and the respective VO-ESD time series.

| Observatory | $\vartheta$ (°) | $\phi$ (°) | $\rho_X$ | $\rho_Y$ | $\rho_Z$ |
|---|---|---|---|---|---|
| CLF | 47.83 | 2.26 | 0.56 | 0.97 | 0.93 |
| DOU | 49.91 | 4.60 | 0.52 | 0.95 | 0.86 |
| FUR | 47.97 | 11.28 | 0.60 | 0.95 | 0.96 |
| ESK | 55.14 | 356.80 | 0.62 | 0.94 | 0.92 |
| HAD | 50.81 | 355.52 | 0.71 | 0.95 | 0.94 |
| LER | 59.97 | 358.82 | 0.40 | 0.87 | 0.80 |
| DRV | −66.53 | 140.01 | 0.62 | 0.14 | 0.83 |
| CZT | −46.24 | 51.87 | 0.72 | 0.90 | 0.98 |

5_v4 (Finlay et al., 2015) time series (accounting for both internal and external fields, in this case only the magnetospheric field) at each 30-day value are also plotted for comparison. This model is an example of the typical SV values on these locations. Our purpose is to determine if the two models show similar long term trends; and also to examine how much external field contributions are present in the VO-ESD time series.

In general the VO-ESD time series follow the same trend as the predictions of CHAOS-5_v4. The latter model exhibits smoother variations, except for *X* in Fig. 11c and d, where the CHAOS-5_v4 model variations are larger than in the VO-ESD time series. For a VO closer to the magnetic pole (Fig. 11a) the CHAOS-5_v4 model shows much smaller short-term variations in *X* and also in *Z* than the VO-ESD prediction.

For all examples, there is a seasonal cycle with one-year period in the *Y* component, especially in Fig. 11a and b. It may be related to the external field annual cycle. Other examples of possible external field contributions to VO-ESD times series are as follows. The high latitude VO (Fig. 11a) shows several short-term temporal vari-

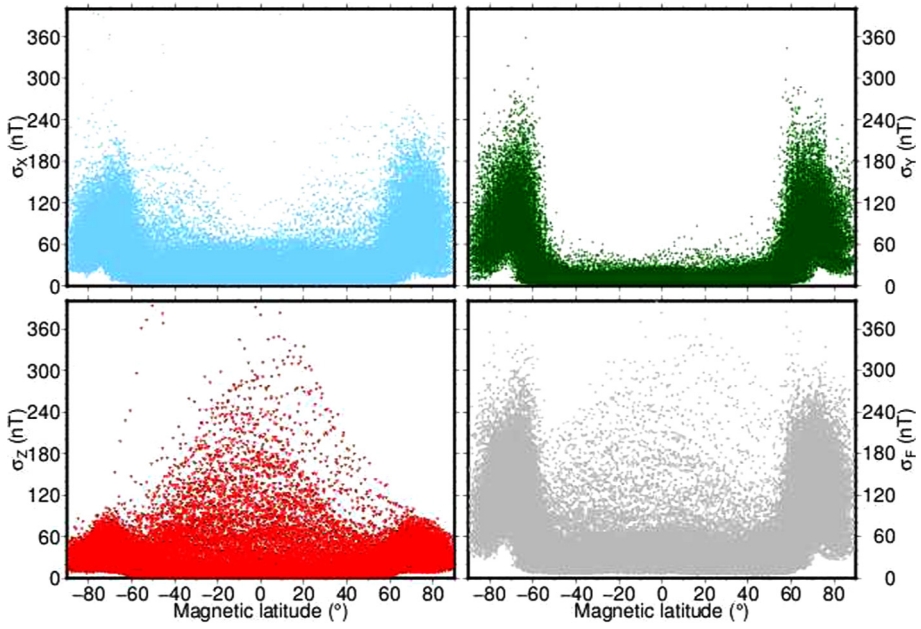


**Fig. 10.** Rms residuals between Swarm measurements and the ESD predictions given by the solution at the selected iteration for all 27 periods and VOs, as a function of the VO (dipole) geomagnetic latitude.

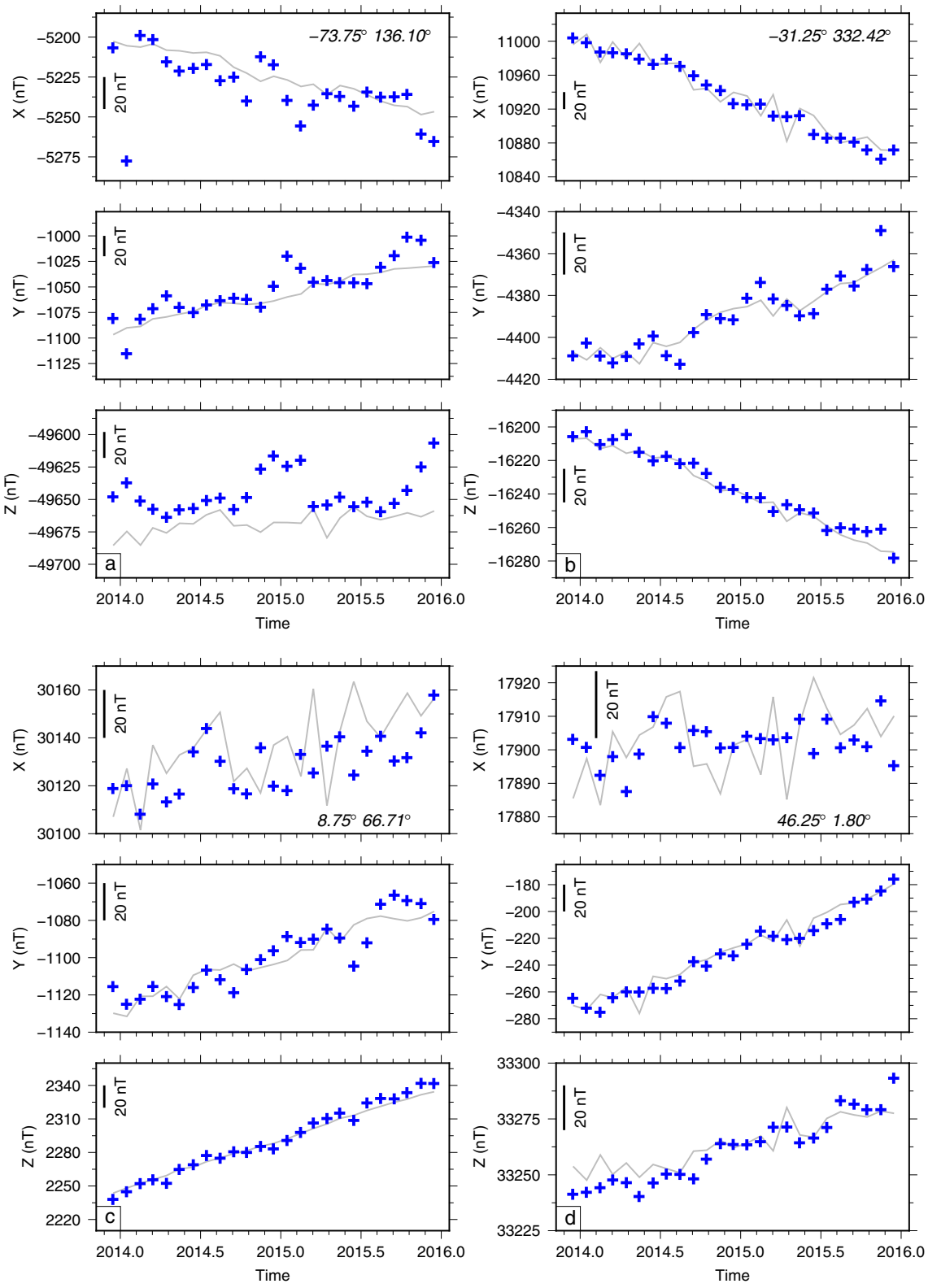


**Fig. 11.** Example of VO-ESD time series (*blue*) and CHAOS-5_v4 predictions at each 30-day period mean time (*gray*) for four VOs. Each VO location is indicated on the *X* component plot, and a scale of 20 nT is displayed at each plot, for comparison between VOs.

ations, coincident for the three magnetic components. One example is around epoch 2015.0, where all three magnetic components show variations of approximately 50 nT. The *X* component shows a sharp variation at the 2nd period of the time series, of more than 25 nT. Closer to the magnetic equator in Fig. 11c, *X* shows several fast short-term variations of up to 30 nT. The *Y* component shows fast short-term possibly repeating variations overlapping a general increasing trend. The large *Z* component rms residuals around the equator do not result in fast or large short-term variations for that component, which increases over the whole period.

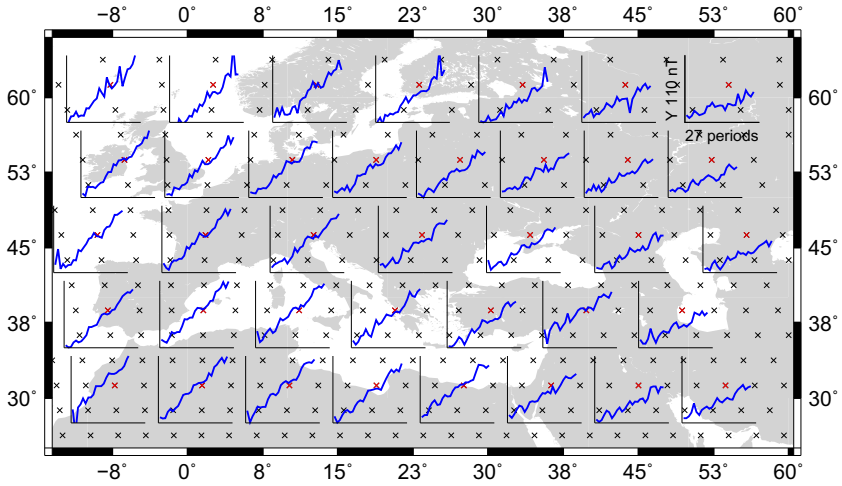


**Fig. 12.** Close-up of the *Y* component VO-ESD time series over Europe during the entire set of periods studied. All VO locations are displayed by black and red symbols, but corresponding time series are only shown for the red ones. (For interpretation of the references to colour in this figure caption, the reader is referred to the web version of this article.)

Fig. 12 shows a close-up over Europe of the *Y* component of the magnetic field as predicted by the VO-ESD approach at satellite altitude (mean value of 495 km) and for twenty-seven 30-day consecutive periods (results for the *X* and *Z* components are displayed in Figs. S1 and S2 of Supplementary Material). For clarity we plot only one out of ten VO time series. The *Y* component increases in all VOs over the considered area. There are however some spatial variations. For example, the VO on the south-west part of the map shows an increase of about 110 nT over the 27 time periods, whereas the central VO increases by less than 90 nT and the north-east VO by less than 50 nT. Actually, from the south-west to the north-east, the temporal variation becomes weaker. Nearby VOs show similar features, such as sharp short-term variations at a given time. Two such examples are the large variation during the second period seen on the south-west VOs; or the large variations during the last periods at the north-east VOs.

## 5. Construction of spherical harmonics models from the VO-ESD time series

Finally, we derive global SH field models from the available VO-ESD time series. Their main characteristics and terminology are indicated in Table 2. The construction of these field models is performed using either one, six or all 30-day period magnetic field values of these time series. Equations describing expansions of internal and external magnetic field potentials in SH can be found in various textbooks (e.g. Langel, 1987; Merrill et al., 1998).

The external magnetic field is important at high latitudes, especially in the horizontal component. As a consequence, only intensity field measurements ($F$) are included in the inversion scheme above 55° geomagnetic latitude, whereas at mid and low latitudes, the three vector components ($X, Y, Z$) are used (see Fig. 10).

The first computed models are snapshots of the magnetic field for only one period, leading to 27 snapshot models, each one based on 6644 VO-ESD values. These models provide a first test of the VO-ESD derived time series, as such models are easier to compare with other SH models than VO-ESD time series. The internal field is considered static up to degree 30 and the external field is described up to degree 2. The snapshot models for one period are denoted VO-ESD_1.TΨ, where Ψ is the number of the model mean period, from 01 corresponding to a mean epoch of 2013.956 to 27 for 2016.126, respectively.

Second, we compute models using data from six consecutive periods. They are denoted VO-ESD_6.TΨ, where Ψ goes from 01 to 22. VO-ESD_6.T01 corresponds to the first six periods (from the mean epoch 2013.956 to the mean epoch 2014.369), VO-ESD_6.T02 contains data from the second period to the seventh (2014.041 to 2014.455 mean epochs) and so on. The secular variation is neglected, so only the static internal and external fields are modelled. The fit to the data is thus expected to be poorer than for single period models. These models aim at further testing the temporal variability of the VO derived time series.

Finally, a model using the full VO-ESD time series (27 periods) is computed. The internal field is computed up to SH degree 30, together with a constant secular variation up to degree 10. The external field is computed up to degree 2 and with no time dependence. For reasons given below a last model with a similar parametrization but using only the last 23 periods is also computed. It is denoted VO-ESD_23.30-10-2. In the following subsections these models are discussed and compared.

**Table 2**
Models terminology, maximum Gauss coefficient degree, number of vector (< 55° absolute magnetic latitude) and scalar (> 55°) input data (corresponding to one value per VO) and associated rms residuals. For both the 1-period and 6-period models the number of input data given are mean values for all respective models.

| Model | *n* maximum | | | Nbr input data | | $\sigma$ (nT) | | | |
|---|---|---|---|---|---|---|---|---|---|
| | MF | SV | Ext. | Vector | Scalar | *X* | *Y* | *Z* | *F* |
| VO-ESD_1.T[01–27] | 30 | 0 | 2 | 5433 | 1211 | see Fig. 13a | | | |
| VO-ESD_6.T[01–22] | 30 | 0 | 2 | 32598 | 7266 | see Fig. 13b | | | |
| VO-ESD_27.30-10-2 | 30 | 10 | 2 | 146691 | 32697 | 9.9 | 6.5 | 10.2 | 11.5 |
| VO-ESD_23.30-10-2 | 30 | 10 | 2 | 104259 | 27853 | 8.8 | 6.2 | 5.6 | 11.4 |

### 5.1. Analysis of the VO-ESD models

We present in Fig. 13a the rms residuals of all 1-period models. Most values are between 2.5 and 5 nT. Two periods, corresponding to the VO-ESD_1.T02 and VO-ESD_1.T04 models, have the largest rms residuals values. For the VO-ESD_1.T02 model all three vector components rms residuals exceed 13 nT, the $Z$ component rms residual is above 33 nT, and the scalar component $\sigma$ is close to 8.5 nT. The VO-ESD_1.T04 model $Z$ component rms residual is 13.6 nT. For the other models, rms residuals are generally between 2.2 and 7.3 nT, except for VO-ESD_1.T01 and VO-ESD_1.T05 which display relatively large $\sigma$, with for example those for VO-ESD_1.T01 around 7.0 nT and for VO-ESD_1.T05 of 8.7 nT. VO-ESD_1.T19 also has horizontal components rms residuals above 7 nT.

Fig. 14a shows geomagnetic power spectra (Lowes, 1974) for all 1-period models. All models have similar power spectra up to degree 13. Beyond this degree, there are considerable differences. The second and fourth 1-period models show power spectra with significantly more energy at small scales. VO-ESD_1.T04 is significantly different from the other 25 models, for degrees 13 to 20. The other 25 models show very similar power spectra, with variations spanning half an order of magnitude, with a small increase towards the higher degrees.

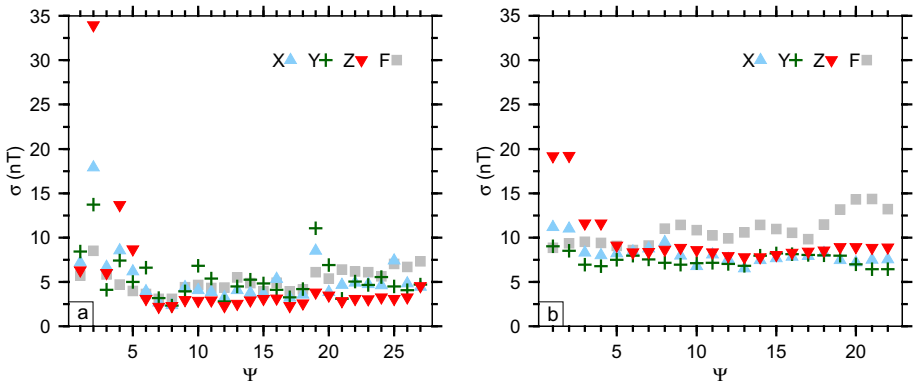


**Fig. 13.** Rms residuals of models (a) VO-ESD_1.TΨ and (b) VO-ESD_6.TΨ, where Ψ is the number of the model period.

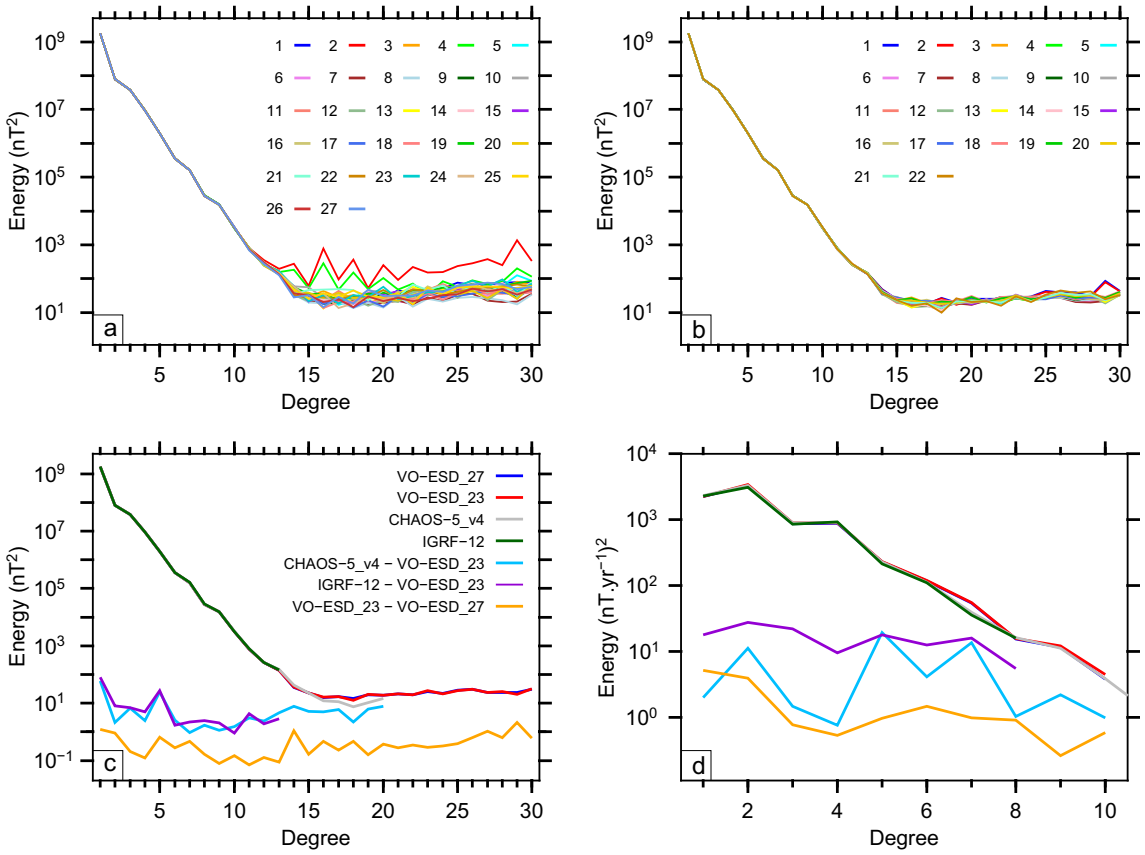


**Fig. 14.** Geomagnetic energy power spectra at the Earth's surface and epoch 2015.0, for (a) all twenty-seven 1-period snapshot models VO-ESD_1.TΨ, (b) all twenty-two 6-period models VO-ESD_6.TΨ, and (c) VO-ESD_27.30-10-2, VO-ESD_23.30-10-2, CHAOS-5_v4 and IGRF-12 models. Secular variation power spectra of models shown in (c) are shown in (d). Also shown in (c) and (d) are the differences between CHAOS-5_v4, IGRF-12 and the VO-ESD_23.30-10-2 model, and the difference between VO-ESD_27.30-10-2 and VO-ESD_23.30-10-2 models. Note that some curves are practically identical and hence overlap.

Fig. 13b presents the rms residuals for the 6-period models. The first two models, VO-ESD_6.T01 and VO-ESD_6.T02, have the largest rms residuals for the $Z$ component, above 19 nT. Their $X$ component rms residuals exceed 10 nT, and $Y$ and $F$ component rms residuals values are between 8.4 and 9.3 nT. VO-ESD_6.T03 and VO-ESD_6.T04 models $Z$ rms residuals exceed 11 nT, the horizontal components $\sigma$ are closer to 8 nT and the scalar component is close to 9.5 nT. For VO-ESD_6.T08 to VO-ESD_6.T22 models, rms residuals for $F$ are in general larger than vector components rms residuals, spanning 9.8 to 14.3 nT. Note that rms residuals of 6-period models are higher than the ones from 1-period models, as expected, as they do not take into account the SV.

Fig. 14b shows the geomagnetic power spectra of the 6-period models. The two first 6-period models (VO-ESD_6.T01 and VO-ESD_6.T02) power spectra differ significantly from the others at degree 29. All models power spectra are practically identical up to degree 13 (Fig. 14b). The power spectra are less dispersed than for 1-period models (Fig. 14a); 1-period may be too short to constrain the field above degree 13.

The first four 30-day periods i.e., VO-ESD_1.T01, VO-ESD_1.T04, VO-ESD_6.T01 and VO-ESD_6.T02, show the largest residuals and significantly different power spectra. This indicates that predictions by the VO-ESD approach are poorer for these periods. These larger rms residuals may be due to Swarm manoeuvres which adjusted the altitude of the three satellites during these periods.

Initially, we computed a model termed VO-ESD_27.30-10-2 using all 27 available periods. However, considering the observed different behaviour during the first four periods, a model from just the last 23 periods was computed, VO-ESD_23.30-10-2. With the subtraction of the first four periods, rms residuals are slightly better for $F$ and $Y$, decreasing from 11.5 to 11.4 nT and from 6.5 to 6.2 nT, respectively. There are larger reductions for $X$, from 9.8 to 8.8 nT, and even more for $Z$ from 10.2 to 5.6 nT (Table 2).

Figs. 14c and d show the main field and secular variation power spectra of the VO-ESD_27.30-10-2 and VO-ESD_23.30-10-2 models, as well as differences between power spectra. For the main field the two power spectra overlap up to degree 13. Their differences are in general below 1 $nT^2$. The differences for each coefficient are always smaller than 0.8 nT (not shown). For the secular variation (Fig. 14d) the power spectra of the differences between VO-ESD_27.30-10-2 and VO-ESD_23.30-10-2 is of the order 5 and 3 $(nT.yr^{-1})^2$ for degrees 1 and 2, respectively, decreasing to approximately 1 $(nT.yr^{-1})^2$ for the other degrees.

Fig. 15 shows the differences at the Earth's surface and epoch 2015.041 (corresponding to $\Psi = 14$), between VO-ESD time series and models VO-ESD_27.30-10-2 or VO-ESD_23.30-10-2 predictions, respectively. Spatial patterns are similar for both models, such as larger differences along the geomagnetic equator for $X$. For $Y$, the residuals are negative in the Pacific zone, contrary to positive ones elsewhere. For $Z$ there is an opposite signal between equatorial and mid-latitudes. Differences over polar areas, for the field intensity (geomagnetic latitude above 55°) are always larger than for other components and latitudes, as it is often the case for satellite based models (Finlay et al., 2015). These spatial biases in the residuals are comparable to those found by Beggan et al. (2009) when looking at residuals based on core flow models derived from SV at virtual observatories.

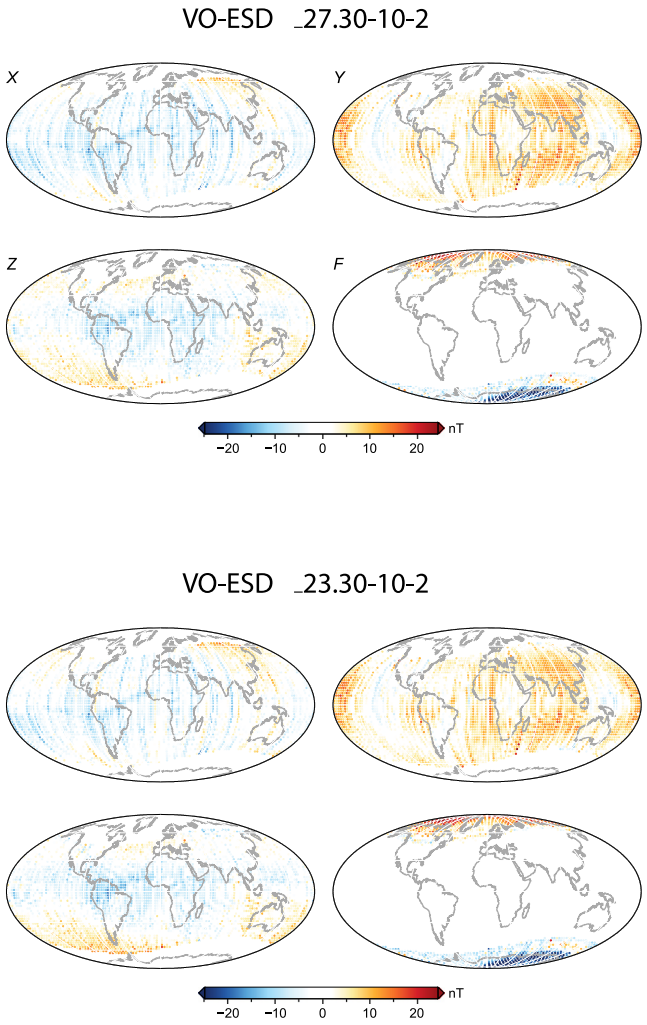


**Fig. 15.** Residuals between the VO-ESD time series used as input data and the models (top) VO-ESD_27.30-10-2 and (bottom) VO-ESD_23.30-10-2 at epoch 2015.041.

### 5.2. Comparison with other models and discussion

We compare the power spectra of our models with those of IGRF-12 (Thébault et al., 2015b) and CHAOS-5_v4 (Finlay et al., 2015). We recall that IGRF-12 is constructed for $n \leqslant 13$ for the main field (MF) and $n \leqslant 8$ for the SV, from a spatial mean of several candidate models (Thébault et al., 2015a), built from ground observatory and satellite measurements. CHAOS-5_v4 uses splines to express the time dependence of Gauss coefficients up to $n \leqslant 20$ for the main and lithospheric fields, and it is constructed from both satellite and ground observatory measurements from more than ten years.

Differences between VO-ESD_23.30-10-2 model power spectra and both IGRF-12 and CHAOS-5_v4 power spectra (Fig. 14) are similar, but not identical. Beyond degree 15, differences between VO-ESD_23.30-10-2 and CHAOS-5_v4 become of the same order of magnitude as the models power spectra themselves. Significant differences exist for degrees 1 and 5, compared to the other degrees. This is especially visible when looking at the differences coefficient by coefficient, as shown in Fig. 16. For the main field, differences between VO-ESD_23.30-10-2 and IGRF-12 are larger than 1 nT for coefficients $g_1^0, h_1^1, g_2^1, g_5^0$ and $h_5^1$. The differences from the CHAOS-5_v4 model are similar.

Fig. 17 shows the differences, at the Earth's surface and epoch 2015.041, between the IGRF-12 and VO-ESD_23.30-10-2 truncated at $n = 13$. Note that the differences to the CHAOS-5_v4 model (Fig. S3, Supplementary Material) are very similar and are not further discussed. The main characteristics are large differences in polar areas, an equatorial antisymmetric difference in $Z$ and an antisymmetric difference between the Atlantic and Pacific areas in $Y$. The $X$ component also presents significant differences along

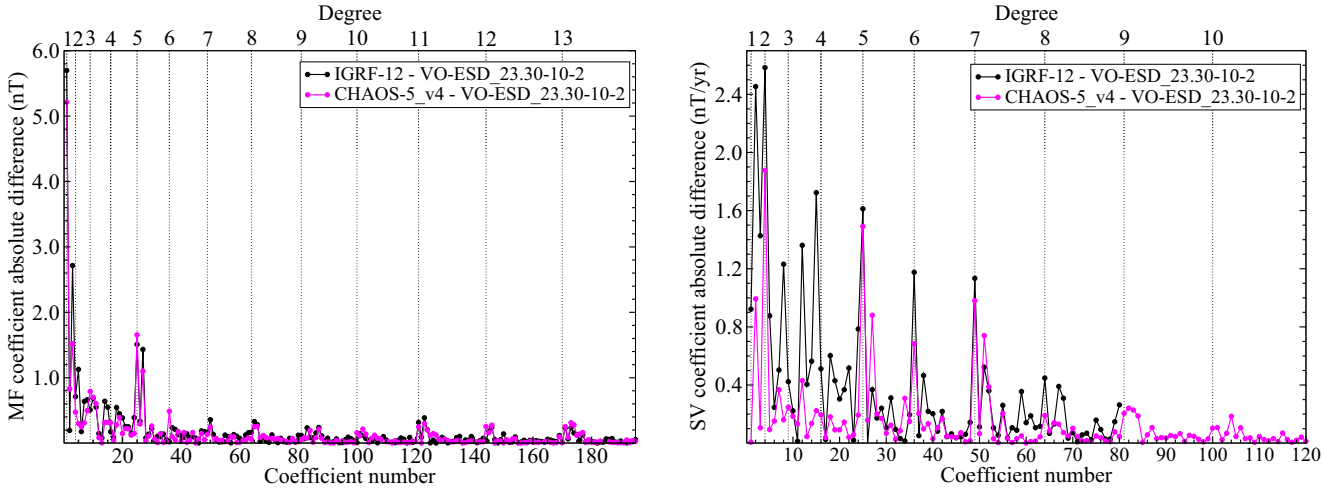


**Fig. 16.** Absolute differences of Gauss coefficients between VO-ESD_23.30-10-2 models and the CHAOS-5_v4 and IGRF-12 models, at epoch 2015.0, and for different SH degrees, for the main field (left) and the secular variation (right).

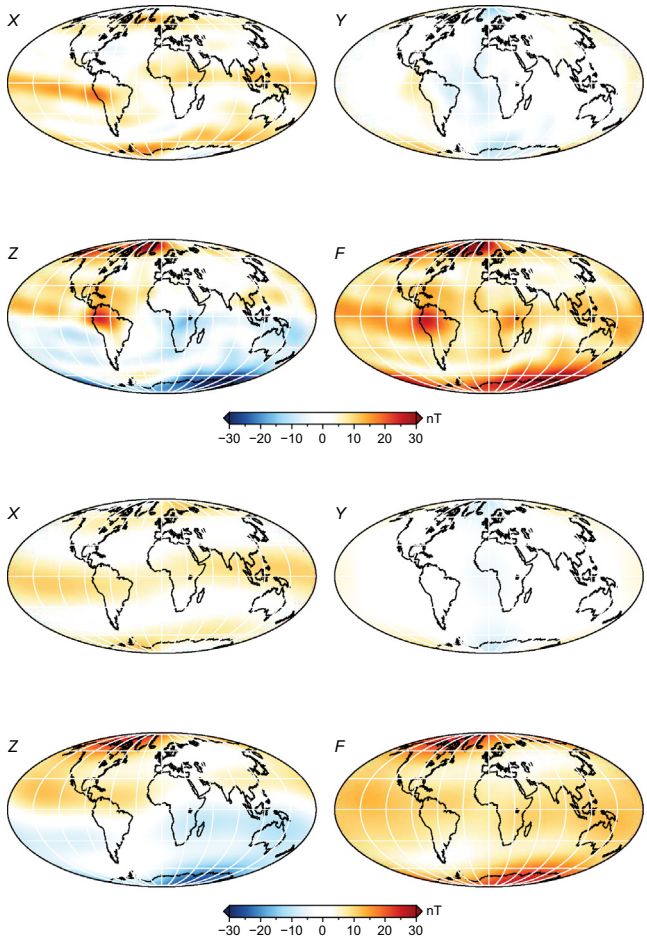


**Fig. 17.** Differences between predictions of IGRF-12 and VO-ESD_23.30-10-2 models, truncated at $n = 13$ (top). Magnetic field components predicted by the differences of the $g_1^0, h_1^1, g_2^1, g_5^0$ and $h_5^1$ coefficients between IGRF-12 and VO-ESD_23.30-10-2 models (bottom). All maps are plotted at the Earth's mean radius and for epoch 2015.041.

the geomagnetic equator. The five largest coefficient differences from IGRF-12 ($g_1^0, h_1^1, g_2^0, g_0^5$ and $h_5^1$) explain around 67% of the signal of the differences, as can be seen in Fig. 17.

The spatial patterns of differences (Fig. 17) may be related to model parametrization and used data set. This is illustrated when looking at some IGRF-12 candidate models (Thébault et al., 2015a) at epoch 2015.0. All used different data sets as well as different modelling strategies. Here we compare some of the candidate models to our models because they were constructed with similar choices. For example, the IZMIRAN team model was the only model using both day and night time magnetic field measurements. It has large differences (close to 2 nT) from the mean of the candidate models at low SH degrees, such as degree 2 or 5 (see Fig. 5 of Thébault et al., 2015a). It also differs from the mean model in the polar areas and along the magnetic equator. It was suggested that these spatial structures along the dip equator result from a contamination of external ionospheric fields, such as the EEJ. As we use day and night time data too, it is likely that ionospheric EEJ leaks into the internal field model and affects the $g_5^0$ and $h_5^1$ coefficients as well. The ISTerre team model (Gillet et al., 2015) presents a significant deviation from the mean model for SH degree 1 (Thébault et al., 2015a). This candidate model is derived from a rather complex parametrization for the internal field, but its external field is explained by a single coefficient, the axial dipole in geomagnetic coordinates, without any Dst dependence (see Eq. (2) of Saturnino et al., 2015). Our VO-ESD derived model does have an external contribution parametrization up to degree 2, but without data selection or Dst dependence. These choices may be the reason for the observed differences at degree 1 between our models and IGRF-12 or CHAOS-5_v4 models.

Ignoring the first four periods of the input data, with VO-ESD_23.30-10-2 model, leads to a slight increase of the difference between the model and both IGRF-12 and CHAOS-5_v4 for the secular variation power spectra (Fig. 14). This can be related to the fact that the time interval to describe the SV is shorter, leading to a possibly poorer SV description. Differences from CHAOS-5_v4 are lower for degrees 4, 8 and 10. No particular coefficient shows a larger difference than others. An interesting point is that coefficients with higher differences are not the same for IGRF-12 and CHAOS-5_v4 models, as seen in Fig. 16. Between VO-ESD_23.30-10-2 and CHAOS-5_v4, differences are higher than 1 nT for coefficients $\dot{g}_2^0$ and $\dot{g}_5^0$; and very close to that value (higher than 0.8 nT/yr) for $\dot{h}_1^1, \dot{g}_5^0, \dot{h}_5^1$ and $\dot{g}_7^0$. It contrasts with the differences from the IGRF-12 model which are higher than 1 nT/yr for several coefficients and even higher than 2 nT/yr for $\dot{g}_1^1$ and $\dot{g}_2^0$ coefficients. Secular variation is constrained as constant and up to SH degree $n = 10$

with the available 27 (or 23) points of the VO-ESD time series. Possibly, this period is too long to consider the secular variation as constant. The parametrization could be improved using for example a B-spline description for the temporal variation.

## 6. Concluding remarks

In this study a new approach to process magnetic satellite measurements is proposed, validated and applied to the first two years of Swarm data. We show that our VO-ESD technique is able to process magnetic field measurements acquired on board orbiting spacecraft and directly extract time series analogous to those at ground observatories. VO volumes are defined as vertical cylinders with vertical extent defined by the altitude of the measurements. No data selection is applied to the measurements. The reduction of the measurements to a common altitude at each VO is done using the Equivalent Source Dipole technique. The measurements inside a VO are fitted by dipole sources homogeneously distributed on an hemispherical mesh placed at the depth of the core-mantle boundary.

When applied to Swarm measurements we find a very good resemblance between ground observatory 30-day means and VO-ESD time series. Computed correlations between VO and surface observations are high, especially for $Y$ component, confirming that the VO-ESD approach is able to extract magnetic field time series similarly to ground observatories.

A global and homogeneous 2.5° resolution mesh of virtual observatory time series is obtained. As at ground observatories, VO-ESD time series display some external field contributions. Despite the very different technique employed to analyse the magnetic field measurements of the Swarm mission, the global SH model we derive is very comparable to previously published models. We notice however that both ionospheric and magnetospheric fields leak into the magnetic field models derived from VO-ESD time series.

The approach could be improved by taking into account external field contributions. One option is to perform prior data selection, by keeping only night time and/or quiet-time measurements. This option has the disadvantage of reducing the number of observations contributing to a given VO. This could be overcome by considering a larger VO volume or a longer time interval. Another option would be to use an a priori correction for the external field with or without a dependence on geomagnetic indices, such as the Dst.

The VO time series we derive should not (yet) be considered as better inputs for SH models. The VO-ESD approach offers nonetheless very promising perspectives. As more magnetic satellite measurements are made available, longer time series can be derived. These can be used, for example, to analyse the global patterns of short-term SV and study sharp temporal variation features such as geomagnetic jerks. In addition, these series could be used to downward continue field and SV to the CMB in order to infer core flows, provided that external magnetic fields are correctly accounted for (Beggan et al., 2009). The VO-ESD approach could also be applied to past (or future) satellite mission measurements, such as CHAMP and Ørsted.

## Acknowledgements

This work was supported by the Centre National des Études Spatiales (CNES) within the context of the project of the "Travaux préparatoires et exploitation de la mission Swarm." It is based on observations with VFM magnetometers embarked on ESA's Swarm mission three satellites. DS was supported by CNES and Région Pays de la Loire. The authors acknowledge ESA for providing access to Swarm Level 1b products. The results presented in this paper rely on data collected at magnetic observatories. We thank the national institutes that support them and INTERMAGNET for promoting high standards of magnetic observatory practice (www.intermagnet.org). C. Finlay is thanked for the RC index needed to compute the CHAOS-5_v4, whose forward code is available at http://www.spacecenter.dk/files/magnetic-models/CHAOS-5. Figures were produced using GMT (Wessel et al., 2013). Finally, we thank two anonymous reviewers for providing constructive comments on this manuscript.

## Appendix A. Supplementary data

Supplementary data associated with this article can be found, in the online version, at http://dx.doi.org/10.1016/j.pepi.2017.06.004.

## References

Baumjohann, W., Nakamura, R., 2007. Magnetospheric contribution to the terrestrial magnetic field. In: Kono, M. (Ed.), Treatise on Geophysics, volume 5, Geomagnetism, Elsevier, Amsterdam, The Netherlands, pp. 77–92.
Beggan, C.D., Whaler, K.A., Macmillan, S., 2009. Biased residuals of core flow models from satellite-derived virtual observatories. Geophys. J. Int. 177, 463–475.
Bloxham, J., Gubbins, D., Jackson, A., 1989. Geomagnetic secular variation. Philos. Trans. R. Soc. London 329, 415–502.
Briggs, B.H., 1984. The variability of ionospheric dynamo currents. J. Atmos. Terr. Phys. 46, 419–429.
Brown, W.J., Mound, J.E., Livermore, P.W., 2013. Jerks abound: an analysis of geomagnetic observatory data from 1957 to 2008. Phys. Earth Planet. Inter. 223, 62–76.
Civet, F., Thébault, E., Verhoeven, O., Langlais, B., Saturnino, D., 2015. Electrical conductivity of the earth's mantle from the first swarm magnetic field measurements. Geophys. Res. Lett. 42, 3338–3346. 2015GL063397.
Covington, J., 1993. Improvement of equivalent source inversion technique with a more symmetric dipole distribution model. Phys. Earth Planet. Inter. 76, 199–208.
Dyment, J., Arkani-Hamed, J., 1998. Equivalent source magnetic dipoles revisited. Geophys. Res. Lett. 25, 2003–2006.
Finlay, C.C., Olsen, N., Tffner-Clausen, L., 2015. DTU candidate field models for IGRF-12 and the CHAOS-5 geomagnetic field model. Earth, Planets Space 67, 114.
Fratter, I., Léger, J.-M., Bertrand, F., Jager, T., Hulot, G., Brocco, L., Vigneron, P., 2016. Swarm Absolute Scalar Magnetometers first in-orbit results. Acta Astronaut. 121, 76–87.
Friis-Christensen, E., Lühr, H., Hulot, G., 2006. Swarm: a constellation to study the Earth's magnetic field. Earth Planets Space 58, 351–358.
Gillet, N., Barrois, O., Finlay, C.C., 2015. Stochastic forecasting of the geomagnetic field from the COV-OBS.x1 geomagnetic field model, and candidate models for IGRF-12. Earth, Planets Space 67, 71.
Gjerloev, J.W., Ohtani, S., Iijima, T., Anderson, B., Slavin, J., Le, G., 2011. Characteristics of the terrestrial field-aligned current system. Ann. Geophys. 29, 1713–1729.
Holme, R., 2015. Large-scale flow in the core. In: Schubert, G. (Ed.), Treatise on Geophysics, Core Dynamics, vol. 8. Elsevier, Oxford, pp. 91–113.
Jackson, A., Jonkers, A.R.T., Walker, M.R., 2000. Four centuries of geomagnetic secular variation from historical records. Philos. Trans. R. Soc. London 358, 957–990.
Katanforoush, A., Shahshahani, M., 2003. Distributing points on the sphere, I. Exp. Math. 12, 199–209.
Kuvshinov, A., Olsen, N., 2006. A global model of mantle conductivity derived from 5 years of CHAMP, Ørsted, and SAC-C magnetic data. Geophys. Res. Lett. 33.
Langel, R.A., 1987. Geomagnetism. In: Jacobs, J.A. (Ed.), chapter 4 – The Main Field, vol. 1. Academic Press, pp. 249–512.
Langel, R.A., Estes, R.H., 1985. Large-scale, near-field magnetic fields from external sources and the corresponding induced internal field. J. Geophys. Res.: Solid Earth 90, 2487–2494. http://dx.doi.org/10.1029/JB090iB03p02487.
Langlais, B., Purucker, M.E., 2007. A polar magnetic paleopole associated with Apollinaris Patera. Planet Spa. Sci. 55.
Langlais, B., Purucker, M.E., Mandea, M., 2004. Crustal magnetic field of Mars. J. Geophys. Res. 109.
Le, G., Lühr, H., Anderson, B.J., Strangeway, R.J., Russell, C.T., Singer, H., Slavin, J.A., Zhang, Y., Huang, T., Bromund, K., Chi, P.J., Lu, G., Fischer, D., Kepko, E.L., Leinweber, H.K., Magnes, W., Nakamura, R., Plaschke, F., Park, J., Rauberg, J., Stolle, C., Torbert, R.B., 2016. Magnetopause erosion during the 17 March 2015 magnetic storm: combined field-aligned currents, auroral oval, and magnetopause observations. Geophys. Res. Lett. 43, 2396–2404.
Lowes, F.J., 1974. Spatial power spectrum of the main geomagnetic field and extrapolation to the core. Geophys. J. R. Astr. Soc. 36, 717–730.
Lühr, H., Park, J., Gjerloev, J.W., Rauberg, J., Michaelis, I., Merayo, J.M.G., Brauer, P., 2015. Field-aligned currents' scale analysis performed with the Swarm constellation. Geophys. Res. Lett. 42, 1–8. 2014GL062453.

Mandea, M., Olsen, N., 2006. A new approach to directly determine the secular variation from magnetic satellite observations. Geophys. Res. Lett. 33.
Maus, S., 2007. CHAMP. In: Gubbins, D., Herrero-Bervera, E. (Eds.), Enc. Geomag. Paleomag.. Springer, Netherlands, pp. 59–60.
Maus, S., Lühr, H., 2005. Signature of the quiet-time magnetospheric magnetic field and its electromagnetic induction in the rotating Earth. Geophys. J. Int. 162.
Mayhew, M.A., 1979. Inversion of satellite magnetic anomaly data. J. Geophys. Z. Geophys. 45, 119–128.
Merrill, R.T., McElhinny, W., McFadden, P.L., 1998. The Magnetic Field of the Earth: Paleomagnetism, the Core, and the Deep Mantle. Acad. Press.
Neubert, T., Mandea, M., Hulot, G., von Frese, R., Primdahl, F., Jørgensen, J.L., Friis-Christensen, E., Stauning, P., Olsen, N., Risbo, T., 2001. Ørsted satellite captures high-precision geomagnetic field data. EOS Trans. Am. Geophys. Union 82, 81–88.
Olsen, N., Mandea, M., 2007. Investigation of a secular variation impulse using satellite data: the 2003 geomagnetic jerk. Earth Planet Sci. Lett. 255.
Olsen, N., Haagmans, R., Sabaka, T.J., Kuvshinov, A., Maus, S., Purucker, M.E., Rother, M., Lesur, V., Mandea, M., 2006. The Swarm End-to-End mission simulator study: a demonstration of separating the various contributions to Earth's magnetic field using synthetic data. Earth Planets Space 58, 359–370.
Olsen, N., Hulot, G., Sabaka, T.J., 2007. The present field. In: Kono, M. (Ed.), Treatise on Geophysics, Geomagnetism, vol. 5. Elsevier, Amsterdam, The Netherlands, pp. 33–75.
Olsen, N., Lühr, H., Finlay, C.C., Sabaka, T.J., Michaelis, I., Rauberg, J., Tffner-Clausen, L., 2014. The CHAOS-4 geomagnetic field model. Geophys. J. Int. 197, 815–827.
Press, W.H., Teukolsky, S.A., Vetterling, W.T., Flannery, B.P., 1992. Numerical Recipes in C (2nd Ed.): The Art of Scientific Computing. Cambridge University Press, New York.
Purucker, M.E., Sabaka, T.J., Langel, R.A., 1996. Conjugate gradient analysis: a new tool for studying satellite magnetic data sets. Geophys. Res. Lett. 23, 507–510.
Reigber, Ch., Lühr, H., Schwintzer, P., 2002. CHAMP Mission Status. Adv. Spa. Res. 30.
Saturnino, D., Langlais, B., Civet, F., Thébault, E., Mandea, M., 2015. Main field and secular variation candidate models for the 12th IGRF generation after 10 months of Swarm measurements. Earth Planets Space 67, 96.
Shewchuk, J.R., 1994. An introduction to the conjugate gradient method without the agonizing pain. Technical report, Pittsburgh, PA, USA.
Sugiura, M., 1964. Hourly values of equatorial $D_{st}$ for the IGY. Ann. Int. Geophys. Year 35, 945–948.
Thébault, E., Finlay, C.C., Alken, P., Beggan, C., Canet, E., Chulliat, A., Langlais, B., Lesur, V., Lowes, F., Manoj, C., Rother, M., Schachtschneider, R., 2015a. Evaluation of candidate geomagnetic field models for IGRF-12. Earth, Planets Space 67, 112.
Thébault, E., Finlay, C.C., Beggan, C.D., Alken, P., Aubert, J., Barrois, O., Bertrand, F., Bondar, T., Boness, A., Brocco, L., Canet, E., Chambodut, A., Chulliat, A., Coïsson, P., Civet, F., Du, A., Fournier, A., Fratter, I., Gillet, N., Hamilton, B., Hamoudi, M., Hulot, G., Jager, T., Korte, M., Kuang, W., Lalanne, X., Langlais, B., Léger, J.-M., Lesur, V., Lowes, F.J., Macmillan, S., Mandea, C., Manoj, S., Maus, N., Olsen, V., Petrov, M., Rother, T.J., Sabaka, D., Saturnino, R., Schachtschneider, O., Sirol, A., Tangborn, V., Taylor, A., Thomson, L., Tffner-Clausen, P., Wardinski Vigneron, I., Zvereva, T., 2015b. International geomagnetic reference field: the 12th generation. Earth Planets Space 67, 79.
Tøffner-Clausen, L., 2013. Swarm Level 1b Product Definition, SW-RS-DSC-SY-0007, Issue 5.15. https://earth.esa.int/documents/10174/1514862/Swarm_L1b_Product_Definition.
Turner, G.M., Rasson, J., Reeves, C., 2007. Observation and measurement techniques. In: Kono, M. (Ed.), Treatise on Geophysics, Geomagnetism, vol. 5. Elsevier, Amsterdam, The Netherlands, pp. 94–143.
Wardinski, I., Holme, R., 2006. A time-dependent model of the earth's magnetic field and its secular variation for the period 1980–2000. J. Geophys. Res.: Solid Earth 111. http://dx.doi.org/10.1029/2006JB004401. B12101.
Wessel, P., Smith, W.H.F., Scharroo, R., Luis, J., Wobbe, F., 2013. Generic mapping tools: improved version released. EOS Trans. Am. Geophys. Union 94, 409–410.